



Ionic liquid-mediated reconstruction of perovskite surface for highly efficient photovoltaics

Ji Hyeon Lee, Benjamin Nketia-Yawson ^{*}, Jae-Joon Lee, Jea Woong Jo ^{*}

Department of Energy and Materials Engineering and Research Center for Photoenergy Harvesting & Conversion Technology (phct), Dongguk University, 30 Pildong-ro, 1-gil, Jung-gu, Seoul 04620, Republic of Korea



ARTICLE INFO

Keywords:

Interface engineering
Ionic liquid
Perovskite photovoltaics
Trap passivation
Interface charge recombination
Hole selective contact

ABSTRACT

To achieve efficient harvesting of light energy, perovskite photovoltaics require a surface passivation process of the perovskite layer. In this study, 1-butylmethylimidazolium hexafluorophosphate ionic liquid was adopted as a surface modifier to passivate a perovskite layer through post-treatment. Results revealed that the ionic liquid effectively reduces surface traps by inducing simultaneous interactions from both cation and anion components. Consequently, the surface treatment with the ionic liquid provided a ~ 15% improvement in the efficiency of the perovskite photovoltaics. However, the formation of perovskite-ionic liquid complex, leading to inefficient charge transport and extraction, was observed when an excess amount of the ionic liquid was used owing to the penetration of the ionic liquid into the photo-active layer. These observations suggest that the ionic liquid should be selectively exposed to the perovskite surface to optimize the efficiency of perovskite photovoltaics treated with ionic liquids.

1. Introduction

In the last decade, perovskite has attracted tremendous attention in photovoltaic applications, and its corresponding devices have achieved the NREL-certified power conversion efficiency (PCE) of 25.7% under simulated sunlight irradiation [1–3]. Recently, perovskite photovoltaics (PPVs) have recorded an efficiency of over 40% in artificial light cells, which have been considered as promising wireless power suppliers for internet of things (IoT) and low-power-driven sensor devices by harvesting indoor light energy during our daily life [4,5]. The promising prospects of perovskite as a light absorber for photovoltaics can be attributed to its extraordinary material properties, such as high optical absorption coefficient [6], fast charge mobility [7], large dielectric constant [8], and long carrier diffusion length [9].

Interfaces between the perovskite and electrodes in PPVs have been recognized as essential parts for completely utilizing the excellent optoelectronic properties of perovskite in photovoltaics. Hence, numerous research have focused on the insertions of electron transport layer (ETL) [10–12] and hole transport layer (HTL) [13–15] to achieve an efficient extraction of photon-generated charge carriers from the perovskite absorber to each electrodes. However, most highly efficient PPVs have been achieved by adopting additional chemical treatments at the

interfaces between the perovskite and charge transport materials. This indicates that the interfaces in PPVs can be optimized by addressing the limited charge extraction and passivation capabilities of charge transport materials by the surface modification of the perovskite layer [16–21]. Accordingly, various candidates, such as amine derivatives [12–25], polymers [26–28], inorganic nanomaterials [29,30], and Lewis acids and bases [31–33] have been explored as surface modifiers in PPVs. Consequently, the effects of these modifiers for blocking unwanted charge carriers [34], reducing energy barriers [35], alleviating surface traps [36], and improving device stability [37] have been reported to date.

Ionic liquid (IL) is another class of chemicals that can actively interact with the perovskite components of PPVs. Particularly, its ionic characteristics formed by the combination of cations and anions enable the replacement and/or passivation of the deficiencies at the surface, grain boundary, and bulk of perovskite [38]. The high potentials of ILs for modifying perovskite precursor solution and ETL in PPVs, and their abilities to achieve controllable crystallization by affecting the intermediate state during the formation of perovskite film [39–41] and efficient charge extraction by modulating the work function and interaction at ETL/perovskite interface have been reported [42–44]. Accordingly, ILs have been employed as surface modifiers to passivate

* Corresponding authors.

E-mail addresses: bnkeyawl@dongguk.edu (B. Nketia-Yawson), whwp78@dongguk.edu (J.W. Jo).

the top surface of the perovskite layer in PPVs. Particularly, ILs can maintain the passivated perovskite/HTL interfaces with tightly bounded forms in the final devices owing to their low solubility in the non-polar solvents used for the fabrication of HTLs, such as chlorobenzene and toluene [45–47]. However, the efficiencies of most IL surface-treated PPVs are lower than those of PPVs treated with commonly-used surface modifiers based on ammonium halide derivatives, including phenethylammonium halides [1] and alkylammonium halides [2,3]. This can be attributed to the differences in the penetration of these modifiers into the underlying perovskite layer during surface treatment and variation in the interactions of the modifier with the top surface of perovskite [48]. Therefore, to further enhance the performance of IL-surface treated PPVs, it is essential to understand the reconstruction of perovskite crystals and the mechanism involved in the interaction formation at the interface of IL-treated surfaces.

In this study, we investigated the effects of surface treatment with IL on the optoelectrical and photovoltaic properties of perovskites by employing 1-butylmethylimidazolium hexafluorophosphate (BMIMPF₆) IL. The introduced IL provided an efficient passivation and a suppressed charge recombination at the interface between perovskite and HTL by the simultaneous formation of interactions between the cation and anion components. Consequently, the IL-surface treated PPVs exhibited improved PCEs of 34.8% under 1000 1× light-emitting diode (LED) illumination and 23.2% under AM 1.5G illumination compared to the control devices (30.1% under LED illumination and 20.1% under AM 1.5G illumination). However, when an excess amount was used for the surface treatment, the IL with ionic and liquidic characteristics penetrated into the photo-active layer, resulting in a degradative conversion of perovskite crystal. Therefore, we demonstrated the importance of the selective reconstruction of perovskite surface during the IL treatment to achieve highly efficient PPVs.

2. Experimental section

2.1. Materials

Lead (II) Iodide (99.99%, trace metal basis [for perovskite precursor]) was supplied from Tokyo Chemical Industry. Formamidinium iodide (>99.99%) (FAI) and methylammonium chloride (>99.99%) (MACl) were obtained from GreatCell Solar. Tin oxide nanoparticle (15% in H₂O) was purchased from Alfa-Aesar. Tin (II) chloride dihydrate (+98%) was purchased from Thermo Fisher Scientific. 2,2',7,7'-Tetrakis[N,N-di(4-methoxyphenyl)amino]-9,9'-spirobifluorene (Spiro-OMeTAD) was purchased from Lumtech (99.8%, sublimed grade). Other unspecified materials were obtained from Sigma-Aldrich.

2.2. Preparation of methylammonium lead tribromide perovskite

Methylamine solution (33 wt% in ethanol) and HBr (48 wt% in H₂O, >99.99%) were mixed at 0 °C. Then, the mixture was allowed to slowly return to room temperature and the reaction was held for 6 hr. After reaction, solvents were removed through rotary evaporator. The resulting crystallites were dissolved in ethanol and then precipitated with diethyl ether. The reprecipitation process was repeated at least twice to obtain pure white solids. Methylammonium bromide (MABr) salts were placed overnight in a vacuum oven for the complete removal of solvents. The obtained MABr was then mixed with PbBr₂ (99.99% trace metals) with a molar ratio of 1:1 at a molar concentration of 1 M in N,N-dimethylformamide (>99.5%) (DMF). After the dissolution, the solution was filtered via syringe filter (0.45 µm PTFE) and dropped into excess volume of toluene. Bright orange precipitates were separated and then washed with toluene and diethyl ether. Methylammonium lead tribromide (MAPbBr₃) powders were dried in a vacuum oven before usage.

2.3. Preparation of ETL

To acquire SnO₂ nanoparticle (NP-SnO₂) layer through spin-coating on pre-patterned indium tin oxide (ITO) substrates, NP-SnO₂ solution (15% in H₂O) was diluted to 2.14 wt% with deionized water and isopropyl alcohol (1:1 v/v) mixture. The diluted NP-SnO₂ solution was spin-coated at 3000 rpm for 30 sec. The NP-SnO₂ films were then annealed in ambient condition at 150 °C for 30 min. For formation of SnO₂ layer through the chemical bath deposition (CBD) method on fluorine doped tin oxide (FTO, Asahi), 137.5 mg of tin (II) chloride dihydrate powder was dissolved in 50 mL of deionized water with 625 mg of urea (98+, Alfa Aesar), 625 µL of HCl (35 wt% in H₂O, Daejung), and 12.5 µL of thioglycolic acid (>97.0%). FTO substrates were placed in the tin chloride solution at 70 °C for 6 hr. After the deposition, the CBD SnO₂ was sonicated with water and isopropyl alcohol for 5 min and annealed at 190 °C for 1 hr. Both NP-SnO₂ and CBD SnO₂ films were treated with 10 mM (aq) of potassium chloride (99.999% trace metal basis) at 3000 rpm for 30 sec and dried at 100 °C for 20 min. Before depositing perovskite layer, NP-SnO₂ on ITO and CBD SnO₂ on FTO were treated with UV-Ozone for 20 min.

2.4. Device fabrication of PPVs

For the fabrication of triple-cation perovskite (CsMAFA), MAFA solution was prepared by dissolving 1.5 M of PbI₂, 1.4 M of FAI, and 0.21 M of MAPbBr₃ in dimethyl sulfoxide (DMSO)/DMF (1:4 v/v) (anhydrous, >99.9%) with an extra 10 mol% of MACl relative to FAI. CsI (99.999% trace metal basis) solution in DMSO (1.5 M) was mixed with MAFA solution at volume ratio of 5:95. For the fabrication of lower bandgap perovskite ((FAPbI₃)_{0.992}(MAPbBr₃)_{0.008}), 1.5 M of PbI₂, 1.4 M of FAI, and 0.0112 M of MAPbBr₃ were dissolved in DMSO/DMF (1:8 v/v) with extra 35 mol% of MACl. Both perovskite precursors were spin-coated on the ETL layers at 1000 rpm for 5 sec (acceleration: 1000 rpm sec⁻¹) and 5000 rpm for 20 sec (acceleration: 4000 rpm sec⁻¹). Before 5 sec of the end of spin-coating, 1 mL of diethyl ether (99.5% GR, Daejung) was dripped. The intermediate films were immediately annealed on a hotplate at 150 °C for 10 min. For the BMIMPF₆ (>97.0%) post-treatment, the IL was diluted in ethyl acetate (99.8%, anhydrous) and spin-coated on the top of perovskite layer at 5000 rpm for 30 sec with subsequent annealing at 100 °C for 5 min. For the deposition of HTL, 100 mg of Spiro-OMeTAD was dissolved in 1.1 mL of chlorobenzene (99.8% anhydrous). Spiro-OMeTAD solution was doped with 23 µL (540 mg mL⁻¹ in acetonitrile) of Li-TFSI (>99.0%), 39 µL of TBP (98%) and 10 µL (376 mg mL⁻¹ in acetonitrile) of FK209 (GreatCell Solar) and then spin-coated at 3000 rpm for 30 sec. The whole fabrication process except the ETL preparation was done in the controlled air condition (relative humidity < 30%, temperature < 25 °C). For the completion of the device, 100 nm of Au was thermally evaporated. The active area (0.091 cm²) of the devices were defined with the pre-patterned mask.

2.5. Characterization of PPVs

The intensity of solar simulator (Xenon lamp, McScience) was calibrated by a standard mono-Si PV device (PVM-396, PV Measurements Inc.) certified by the National Renewable Energy Laboratory. Hysteresis index (HI) was calculated from the equation of (P_{max,rev} - P_{max,fwd})/P_{max,rev}. Measurement under artificial light (5000 K LED lamp) was done with the home-made set-up. Artificial light intensity was modulated via voltage transformers (Hwaseong) and the irradiance was monitored by spectrophotometer (AvaSpec-ULS2048XL-EVO). External quantum efficiency (EQE) spectra were measured via photo-modulation spectroscopy (McScience, K3100 Spectral EQE Measurement System) under a monochromatic xenon light source with calibration using a Si photodiode certified by the National Institute for Standards and Technology. The current density–voltage (J–V) measurement under the simulated lights was performed from 1.4 to –0.1 V with scan rate of 150 mV sec⁻¹. Diode

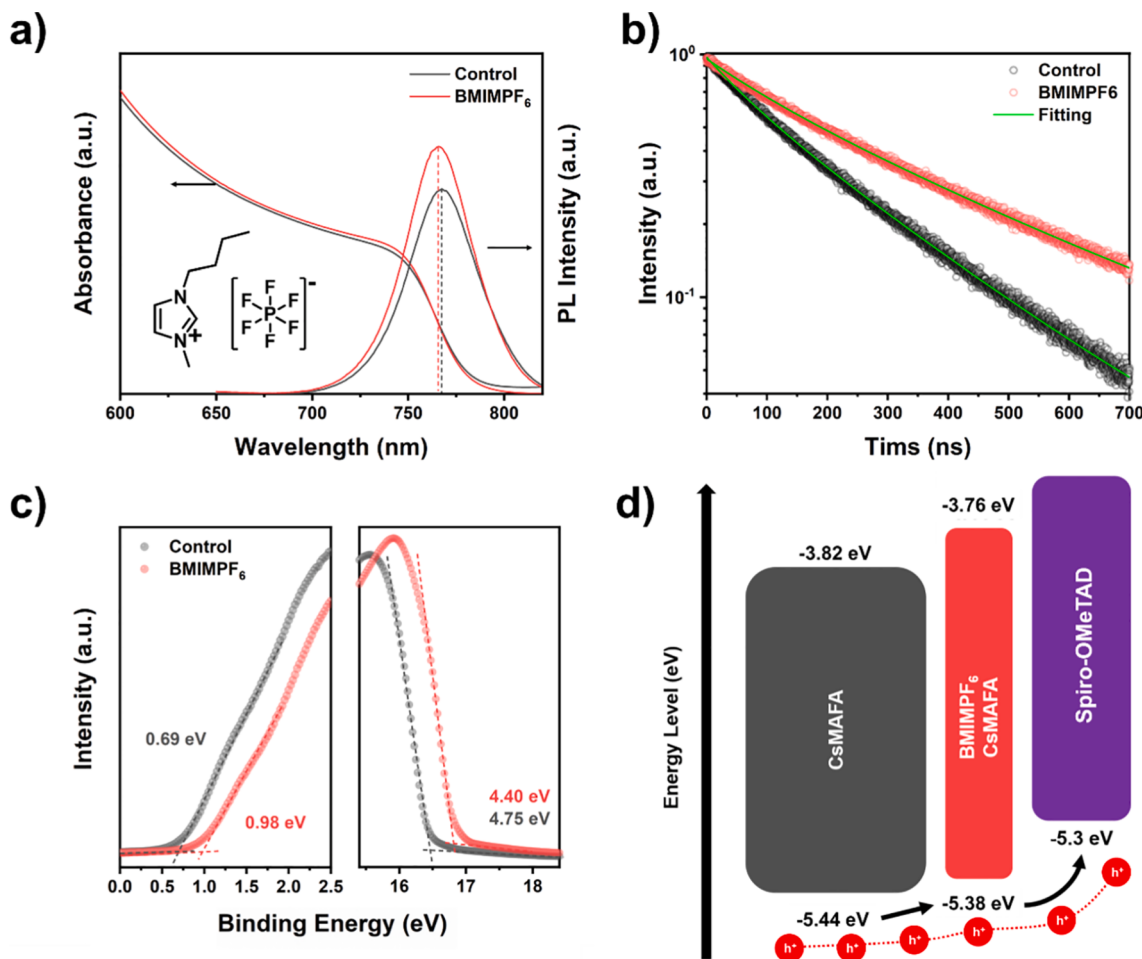


Fig. 1. a) UV-Vis absorption and steady-state photoluminescence (PL) spectra of the control and the BMIMPF₆-treated CsMAFA perovskite films on bare glasses. The inset show chemical structure of the ionic liquid. b) Time-resolved PL spectra of the control and BMIMPF₆-treated CsMAFA perovskite films on bare glasses. c) Ultraviolet photoelectron spectroscopy spectra of the CsMAFA perovskite films before and after the BMIMPF₆ treatment. d) Schematic illustration of the energy levels between CsMAFA perovskite and HTL.

ideality factor (n) was extracted from the equation: $n = (q/k T)(dV_{OC}/dlnP_{in})$, where q is the elementary charge, k is the Boltzmann constant, T is the absolute temperature and P_{in} is the power density of input light. Hole-only perovskite devices were fabricated with the device configuration of ITO/poly(3,4-ethylenedioxythiophene):poly(styrenesulfonate) (PEDOT: PSS)/perovskite/polymer/Au. Trap density was estimated from the trap-filled limit voltage (V_{TFL}) region of the resulting curve under dark current according to the equation: $V_{TFL} = (q n_t L^2)/(2 \epsilon_r \epsilon_0)$, where L is the thickness of active layer, q is the elementary charge, ϵ_r is the relative dielectric constant of the perovskite layer, ϵ_0 is the vacuum permittivity, n_t is the defect density. Impedance analysis was carried out using Autolab PGstat12 potentiostat with an impedance module in the frequency range of 0.1 Hz ~ 1.5 MHz with a perturbation amplitude of 10 mV. Zview software was used for fitting the obtained impedance spectra with appropriate equivalent circuit.

2.6. Characterization of perovskite films

UV-Vis absorption spectra were obtained using Scinco S-3100. The surface morphologies and potential energy of films were investigated via tapping-mode atomic force microscopy (AFM) (Asylum). The same device was used for Kelvin probe force microscopy (KPFM) measurement. Steady-state photoluminescence (PL) were measured with Agilent Cary Eclipse fluorescence spectrophotometer (Varian). Time-resolved PL (TR-PL) measurements were performed using a single photon counting system coupled with a single photon counting detector (wavelength of laser

source for excitation = 435 nm) (FlouTime 300, PicoQuant). The morphologies of perovskite films were identified using scanning electron microscopy (SEM) (Hitachi S-3000 N). X-ray diffraction (XRD) data were measured with Ultima IV (Rigaku). X-ray photoelectron spectroscopy (XPS) plots were measured with Veresprobe II (ULVAC-PHI). X-ray beam size was 100 μm with energy source of monochromatic Al K α . The same device was used for Ultraviolet photoelectron spectroscopy (UPS) measurement with a bias of -10 V under He (I) gas.

3. Results and discussion

In this study, BMIMPF₆ IL [49–52] composed of large sized-ions without perovskite components, such as methylammonium and halide, was used as the surface modifier. This IL was selected based on the fact that it would enable a further understanding of the mechanism involved in the IL treatment of PPVs by excluding the effects of the replenishing insufficient components and the dimensional change in the perovskite layer during surface treatment. Additionally, BMIMPF₆ IL has been previously investigated as an ETL modifier and has been demonstrated to provide improved contacts between ETL and perovskite by forming gradient energetic barriers and facilitating electron extractions [53,54]. For the surface treatment with IL, BMIMPF₆ was diluted in ethyl acetate (2.5 mM) and spin-coated on the top surface of perovskite at 5000 rpm for 30 s, followed by thermally annealing at 100 °C for 5 min (See Experimental section). Fig. 1 shows the optoelectrical properties of Cs_{0.05}(FA_{0.85}MA_{0.15})_{0.95}Pb(I_{0.87}Br_{0.13})₃ triple-cation perovskite

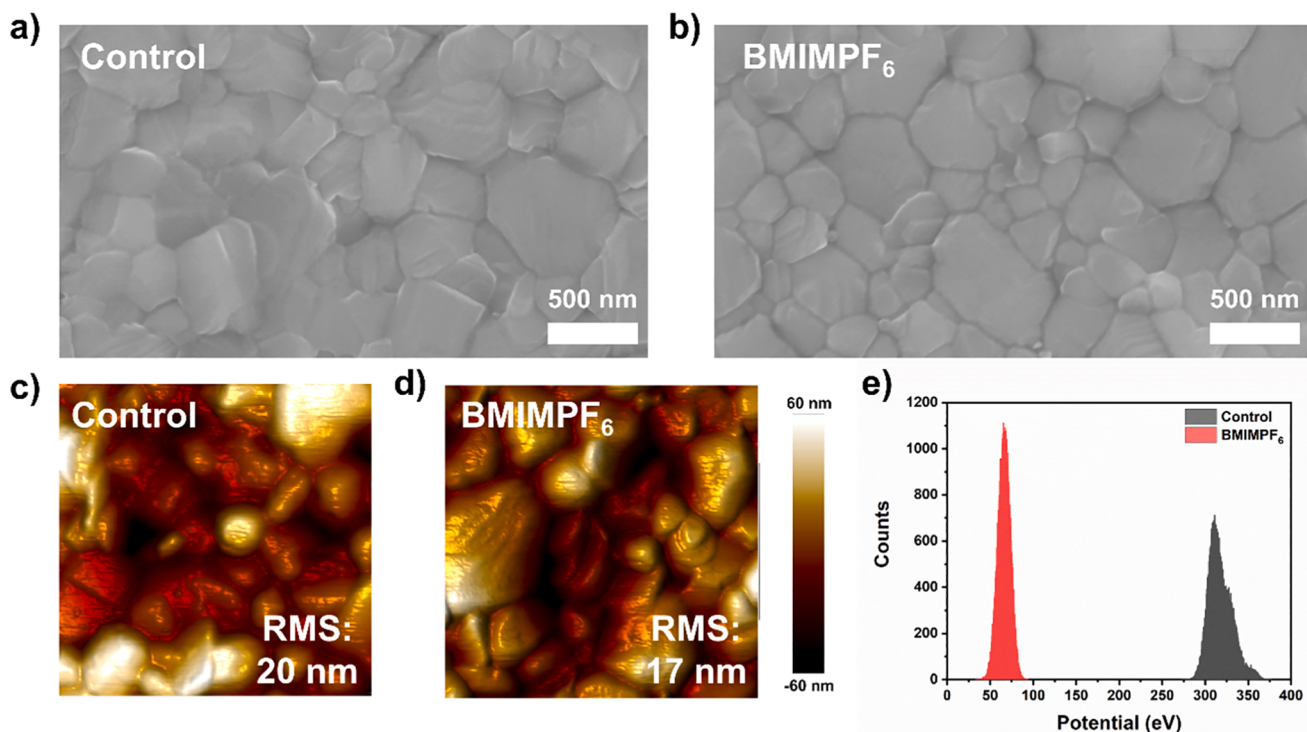


Fig. 2. Top surface scanning electron microscopy (SEM) images of the a) control and b) BMIMPF₆-treated CsMAFA perovskite films. Topographic atomic force microscopy images of the c) control and d) BMIMPF₆-treated CsMAFA perovskite films ($2 \mu\text{m} \times 2 \mu\text{m}$). e) Contact potential difference distributions of the control and BMIMPF₆-treated CsMAFA perovskite films ($2 \mu\text{m} \times 2 \mu\text{m}$) obtained using Kelvin probe force microscopy measurement.

(CsMAFA, MA = methylammonium, FA = formamidinium) films before and after the BMIMPF₆ IL treatment. There was no notable difference in the UV–Vis spectra of both perovskite films, and Tauc equation ($\alpha h\nu = A(h\nu - E_g)^n$, where α is the absorbance coefficient, ν is the incident photon frequency, h is the plank's constant, A is the proportionality constant, E_g is the optical band edge, and n is 1/2 of the direct band transition)

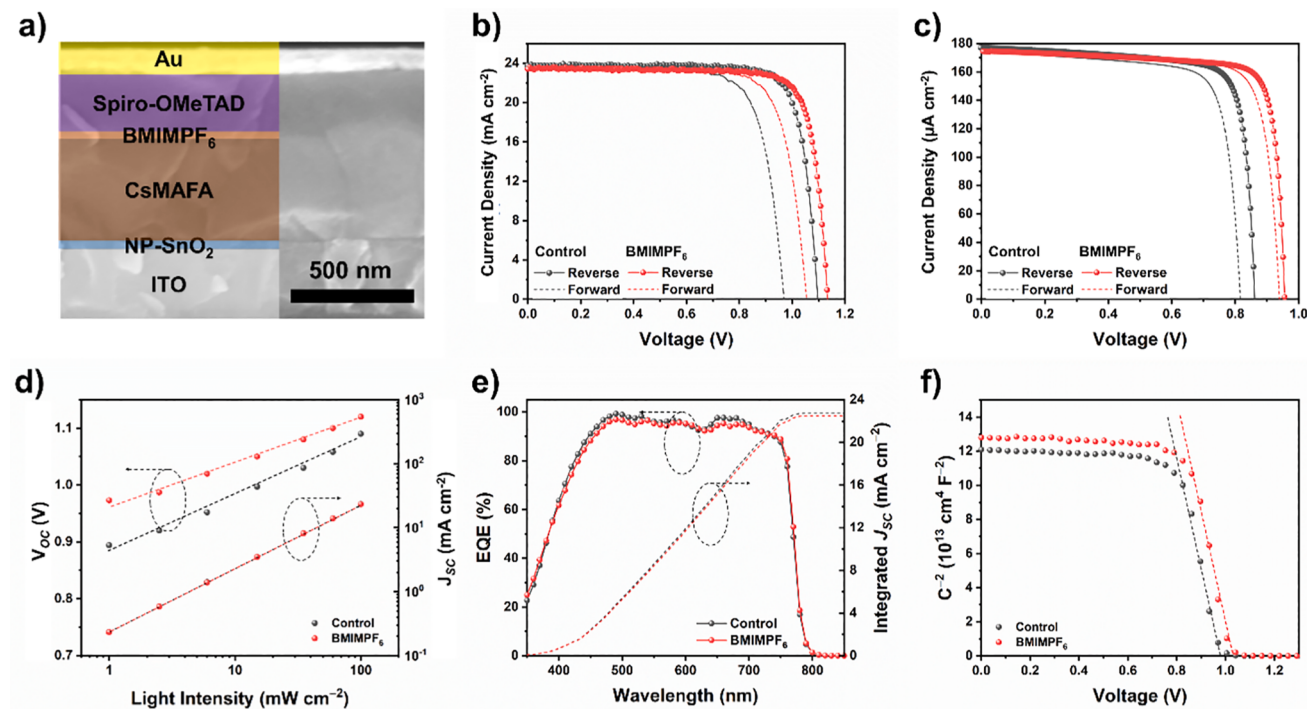


Fig. 3. a) Cross-sectional SEM image of CsMAFA PPV with a device architecture. Current density–voltage (J – V) characteristics of the CsMAFA PPVs under b) AM 1.5G (100 mW cm^{-2}) and c) 5000 K LED ($1000 \text{ lx}, 3.71 \mu\text{A cm}^{-2}$) illuminations. d) Light intensity-dependent V_{OC} and J_{SC} of the PPVs before and after the BMIMPF₆ treatment. e) Corresponding external quantum efficiency (EQE) spectra of the CsMAFA PPVs fabricated using the control and BMIMPF₆-treated perovskites. f) Mott–Schottky plots of the PPVs obtained at 100 kHz without an electron transport layer.

Table 1

Photovoltaic parameters of the control and the BMIMPF₆-treated CsMAFA PPVs under AM 1.5G and 5000 K LED illuminations.

Surface treatment	Scan direction	V _{OC} [V]	J _{SC} [mA cm ⁻²]	FF [%]	PCE [%]	R-F average PCE [%]
AM 1.5G (100 mW cm ⁻²)						
Control	Rev	1.10	23.8	81.2	21.2	19.3
	Fwd	0.98	23.7	75.5	17.3	
BMIMPF ₆	Rev	1.13	23.4	81.3	21.6	20.4
	Fwd	1.06	23.6	77.0	19.2	
5000 K LED (1000 lx, 3.71 μA cm ⁻²)						
Control	Rev	0.86	0.176	77.7	31.5	30.1
	Fwd	0.81	0.173	75.8	28.6	
BMIMPF ₆	Rev	0.95	0.174	80.2	35.8	34.8
	Fwd	0.93	0.175	77.2	33.9	

revealed that the two films exhibited almost identical bandgaps of 1.62 eV (Fig. 1a). In contrast, the steady-state PL spectra revealed that compared to the control perovskite film without surface treatment (emission peak = 767 nm), the BMIMPF₆-treated perovskite film exhibited an increased PL intensity and a hypsochromic shift in the emission peak to 765 nm. This would indicate that the surface treatment with BMIMPF₆ IL resulted in a reduction in the shallow energy traps of perovskite. [55] It has been reported that the traps near band edges within perovskite possibly offer a red-shifted emission peak through the radiative recombination between trap states [17,21,32,33,46]. The reduced traps on the BMIMPF₆-treated perovskite surface were further verified by TR-PL analysis, and the results are shown in Fig. 1b. When the TR-PL decay were fitted using a bi-exponential function, the BMIMPF₆-treated perovskite film exhibited a prolonged PL lifetime of 345 ns compared to the pristine films (222 ns) (Table S1). This result demonstrated a suppression of the non-radiative recombination in the BMIMPF₆ treated-perovskite film [56,57]. Moreover, UPS was conducted to explore the influence of IL treatment on the energy levels of perovskite (Fig. 1c). The results revealed that the BMIMPF₆ treatment provides the formation of perovskite surface with shallower energy levels and a shift in the valence band maximum from -5.44 to -5.38 eV. This was probably attributed to the induced dipole formed by the attached IL [58], and the band shift would contribute to efficient hole transfer at the perovskite/HTL interface in PPVs (Fig. 1d) [59,60].

The morphologies of the perovskite films before and after the IL treatment were investigated using SEM. After the BMIMPF₆ treatment, the treated perovskite films maintained their average grain size of 400–500 nm without notable difference (Fig. 2a and b; Fig. S1). The similar morphologies of the perovskite films before and after IL treatment were further verified by AFM, and the results are shown in Fig. 2c and d. In contrast, the BMIMPF₆ treatment afforded a reduction in the root-mean-square (RMS) roughness of the perovskite surface from 20 to 17 nm, suggesting that the IL with a polar nature flattened the top surface of the perovskite during the treatment. This smooth surface would be beneficial for the effective contact between perovskite and HTL [61,62]. Fig. 2e shows the contact potential difference (CPD) statistics of the control and BMIMPF₆-treated perovskite films obtained using KPFM under dark conditions. The CPD of the BMIMPF₆-treated perovskite film shifted to lower values compared to that of the control film. This implies that the BMIMPF₆ treatment reduced the energy level differences between the surface potential of perovskite and the work function of the tip, which also supports the shift in the energy levels of perovskite to shallower values observed in the UPS measurement (Fig. 1d). Furthermore, the calculated full width at half maximum (FWHM) of CPD of the control and the BMIMPF₆-treated perovskite films were 29.2 and 17.5 eV, respectively (Fig. S2). This decrease in the FWHM of the CPD of the IL-treated perovskite films would alleviate the broadness of the regional energy barrier at the perovskite/HTL interface, resulting in more homogeneous hole extraction and transfer from perovskite to HTL.

The photovoltaic performances of the PPVs prepared using the control and the BMIMPF₆-treated CsMAFA perovskites were investigated using the planar heterojunction architecture of ITO/NP-SnO₂/CsMAFA/Spiro-OMeTAD/Au (Fig. 3a). The J-V characteristics of PPVs measured under AM 1.5G (100 mW cm⁻²) and 5000 K LED (1000 lx, 3.71 μA cm⁻²) illuminations are shown in Fig. 3b and c, and their photovoltaic parameters are summarized in Table 1. Under AM 1.5G illumination, the control and BMIMPF₆-treated PPVs exhibited comparable short-circuit current density (J_{SC}) of ~ 23.6 mA cm⁻² and a fill factor (FF) of 81%. However, in the reverse scan, the BMIMPF₆-treated PPV exhibited an improved PCE of 21.6% with an enhanced open-circuit voltage (V_{OC}) of 1.13 V compared to that of the control device (PCE = 21.16% and V_{OC} = 1.09 V). These improved efficiency and V_{OC} of the BMIMPF₆-treated PPV may be attributed to the passivation of the perovskite surface and the reduced charge recombination at the perovskite/HTL interface after the IL treatment. Similarly, the PCE enhancement of the IL-treated PPVs was also observed under low-intensity 1000 lx.

LED illumination. The BMIMPF₆-treated PPV exhibited an improved PCE of 35.8% with a V_{OC} of 0.95 V and a FF of 80.2% compared to the control device with a PCE, V_{OC}, and FF of 31.5%, 0.86 V, and 77.7%, respectively. Statistical data with 20 individual devices are shown in Fig. S3 and Table S2. The more notable improvement in the efficiency of the IL-treated PPV under dim light illumination could be attributed to the fact that the trap-assisted recombination is dominant for low power extraction in PPVs [63,64]. The improved performances of PPVs after the IL treatment was further investigated by extracting the ideality factor (*n*) and the power factor (*α*) from the light intensity-dependent V_{OC} and J_{SC}, as shown in Fig. 3d. Compared to the control device (*n* = 1.64), the BMIMPF₆-treated PPV exhibited a lower *n* value of 1.23, which corresponds to the reduced charge recombination of the IL-treated PPV compared to that of the control counterpart. An ideality factor close to 1 corresponds to a suppressed charge recombination [65]. In contrast, the control and BMIMPF₆-treated PPVs exhibited similar *α* values of ~ 0.98, suggesting that the IL treatment had no effect on the charge transport and extraction ability of PPV at the short-circuit condition. The corresponding EQE spectra of the PPVs exhibited similar characteristics (Fig. 3e). The control and BMIMPF₆-treated PPVs exhibited integrated current densities of 22.8 and 22.5 mA cm⁻², respectively, which were consistent with the J_{SC} values of the PPVs under AM 1.5G condition. The slightly reduced J_{SC} in the PPV with the BMIMPF₆ treatment is possibly due to the bulky size of BMIMPF₆, which may induce the charge accumulation by retarding the charge transfer at the perovskite/HTM interface. The enhanced V_{OC} of the IL-treated PPV was investigated using Mott–Schottky plot obtained at 100 kHz without ETL. As shown in Fig. 3f, the onset potential of the decrease in the capacitance of the PPV shifted to a higher potential value after the BMIMPF₆ treatment, corresponding to an increased built-in potential of the IL-treated device.

The device stability of the unencapsulated PPVs were tested under ambient conditions (relative humidity = 25–35%), and the results are shown in Fig. S4. After exposure for 1000 h, the efficiency of the control device decreased by ~ 15%, whereas the BMIMPF₆-treated PPV retained approximately 97.6% of its original PCE. To validate the effect of BMIMPF₆ treatment on the operational stability of PPV, maximum power point (MPP) tracking was performed. The control device exhibited rapid degradation under AM 1.5G illumination with 0.9 V bias and its power decreased to 80% of original value after 180 min. In contrast, the BMIMPF₆-treated PPV provided a highly stable operation with a constant power output for up to 460 min, and its power values reached 80% of its original output after 1257 min, which corresponded to approximately 7-fold increased time for the device degradation compared to that of the control device. (Fig. S4b) This results indicated that the BMIMPF₆ IL treatment of the perovskite surface enhanced the device stability of PPV.

The interaction between perovskite and BMIMPF₆ IL was explored by

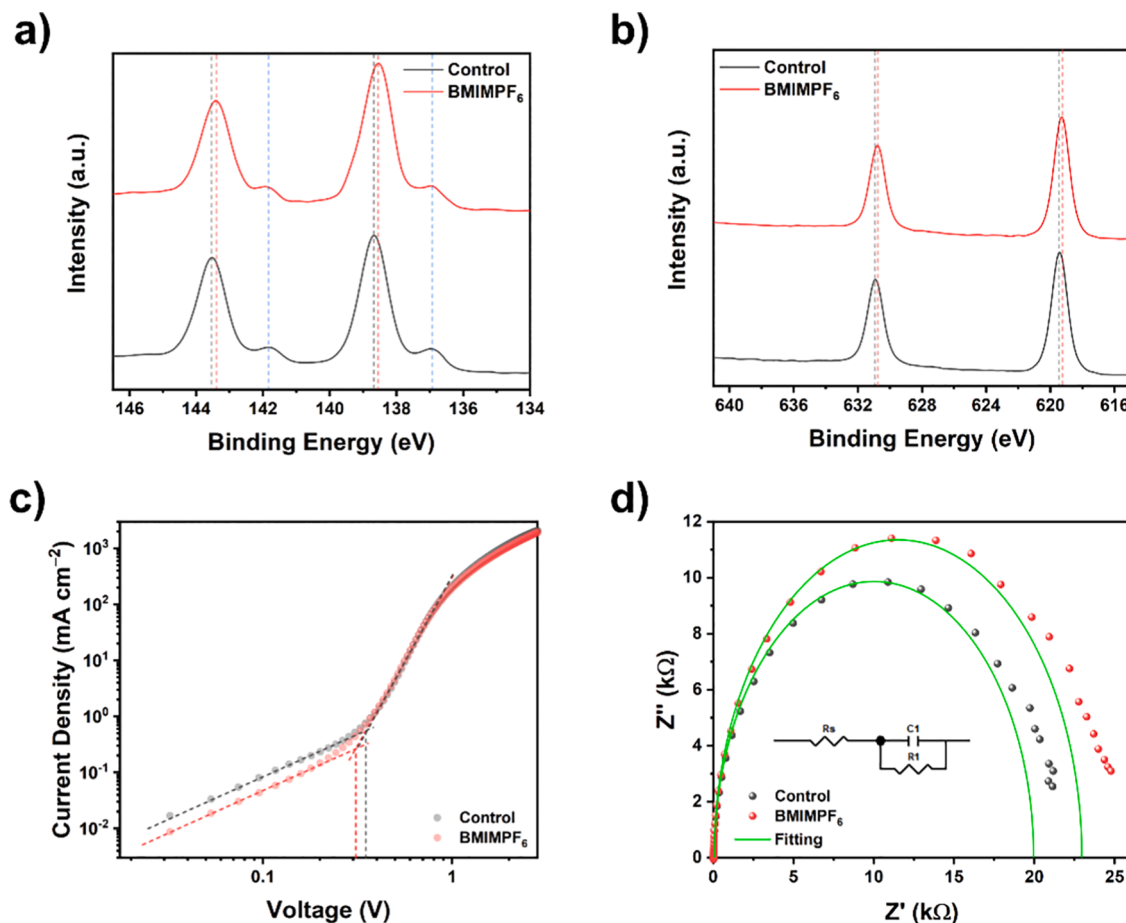


Fig. 4. a) Pb 4f and b) I 3d X-ray photoelectron spectroscopy profiles of the CsMAFA perovskite films before and after the surface treatment with BMIMPF₆ IL. c) Dark J–V curves of the hole-only perovskite devices with a device architecture of ITO/PEDOT:PSS/CsMAFA/Spiro-OMeTAD/Au. d) Nyquist plot of CsMAFA PPVs measured under dark condition. The inset shows the equivalent circuit.

performing XPS, and the XPS profiles are shown in Fig. 4a and b. The Pb²⁺ peaks of *f*_{5/2} and *f*_{7/2} were observed in the Pb 4f spectra of the control perovskite at 143.5 and 138.7 eV, and the two peaks corresponding to the metallic Pb⁰ were observed at 141.8 and 136.9 eV. The XPS pattern of the BMIMPF₆-treated perovskite maintained the similar characteristics of the Pb²⁺ and Pb⁰ peaks, and there was no significant shift in the binding energies of the metallic Pb⁰ peaks. However, the Pb²⁺ peaks of *f*_{5/2} and *f*_{7/2} shifted to lower binding energies by -0.1 eV shifts. Similarly, the I 3d_{3/2} and I 3d_{5/2} peaks of perovskite also shifted from 630.9 to 630.7 eV and from 619.4 to 619.2 eV, respectively, after the BMIMPF₆ treatment. This observation suggests that the surface treatment of perovskite film with BMIMPF₆ IL could passivate the Schottky defects of A-site cation and X-site anion on the perovskite surface through the formation of interactions between BMIMPF₆ and perovskite [66–68]. Subsequently, the hole trap densities of the control and BMIMPF₆-treated PPVs were identified using the space charge limited current (SCLC) method by fabricating hole-only devices with an architecture of ITO/PEDOT:PSS/CsMAFA/Spiro-OMeTAD/Au. As shown in Fig. 4c, the device fabricated using the BMIMPF₆-treated perovskite exhibited a reduced trap density of $3.02 \times 10^{15} \text{ cm}^{-3}$ with a slightly lower *V*_{TFL} of 0.307 V compared to those of the control device (*trap density* = $3.43 \times 10^{15} \text{ cm}^{-3}$, *V*_{TFL} = 0.350 V) (Table S3). This result confirmed the efficient ability of BMIMPF₆ IL to passivate the traps.

on the perovskite surface, which would enhance the photovoltaics performances of the IL-treated PPVs by suppressing the charge recombination with the reduced trap density at the perovskite/HTL interface [69–71]. The charge recombination characteristics of the PPVs before and after the IL treatment were further probed using electrochemical

impedance spectroscopy (EIS) [72,73]. Fig. 4d shows the Nyquist plot of the control and BMIMPF₆-treated PPVs under dark condition with a forward bias voltage of 0.8 V. Distinct semicircles were observed in the Nyquist plot of both devices, indicating the existence of charge recombination in the PPVs. However, the BMIMPF₆-treated PPV exhibited a larger recombination resistance (R₁) of 22.9 kΩ compared to that of the control device (R₁ = 19.9 kΩ) (Table S3). This increased resistance against the charge recombination within the PPV after the IL treatment was consistent with the prolonged charge-recombination lifetime of the IL-treated perovskite observed in the TR-PL analysis (Fig. 1b).

To gain deeper insight into the mechanism of the IL treatment, the characteristics of the perovskites depending on the concentration of the IL solution used for the surface treatment were investigated. The measurement of the photovoltaics performances of the PPVs revealed that the BMIMPF₆ treatment at a concentration of 2.5 mM provides the optimized performance of the PPVs (Fig. S5 and Table S4). In case of the BMIMPF₆ IL, both cation and anion were believed to actively coordinate with the perovskite surface owing to the polar characteristics of ion: Imidazole-based cation attached to the lead component through the formation of nitrogen-lead interaction [74]; PF₆ anion possibly acted as a counter cation of the ammonium component on the perovskite surface through anion exchange [75]. However, this polar and liquidic IL could also easily penetrate the underlying perovskite film without attaching to the surface, which potentially induces the degradation and phase transformation of perovskite. To elucidate the mechanism involved in the interaction of the IL with perovskite, XRD analysis of the perovskite films treated with various concentration of BMIMPF₆ in ethyl acetate solution for the surface treatment was performed. With an increase in

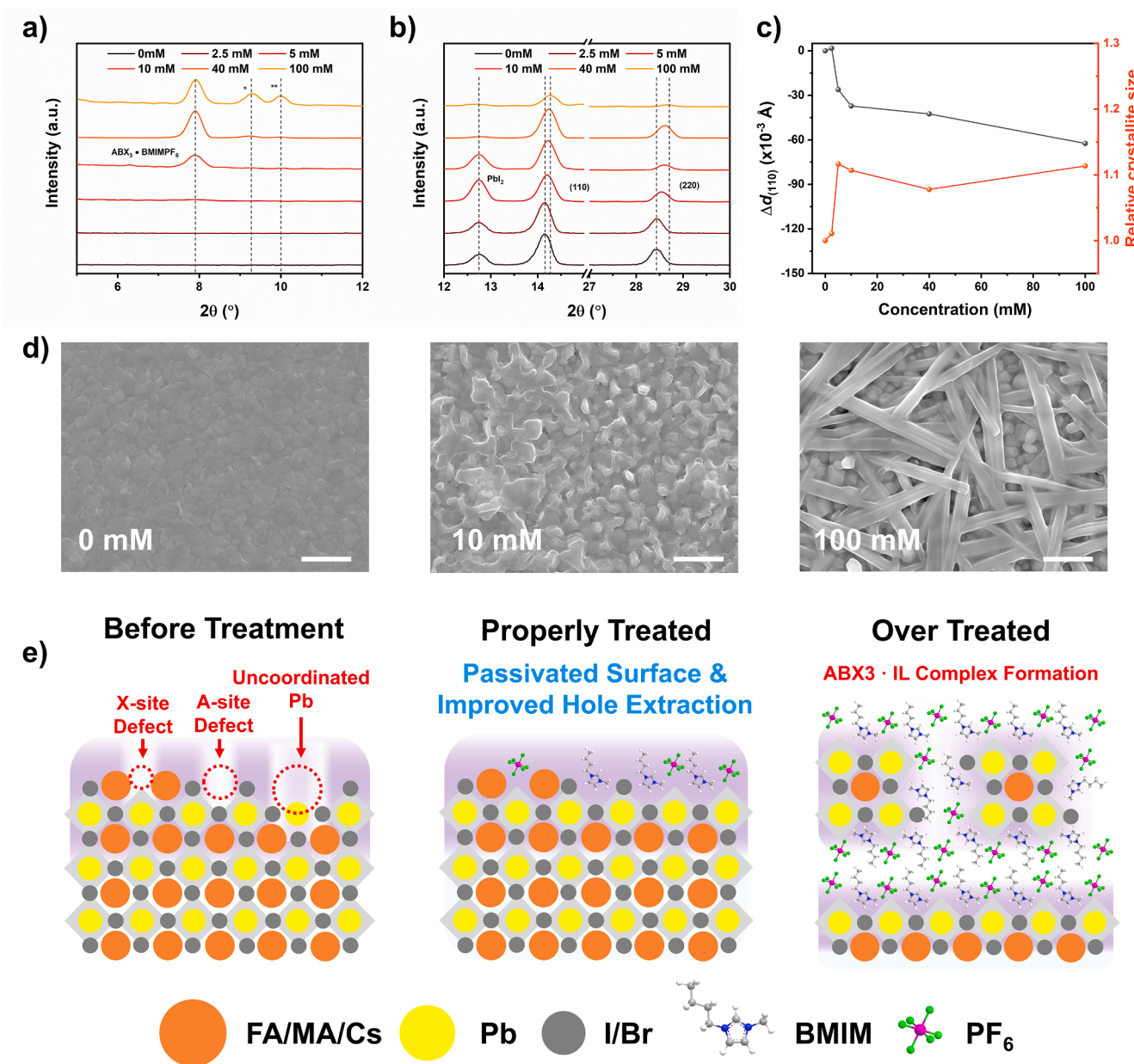


Fig. 5. a,b) X-ray diffraction spectra of the CsMAFA films treated with various concentration of BMIMPF₆ IL in ethyl acetate solution. c) Differences in the $d_{(110)}$ of the CsMAFA films before and after the BMIMPF₆ treatment and relative crystallite size depending on the concentration of the IL solution used for surface treatment. d) SEM images of the CsMAFA films treated with various concentration of BMIMPF₆ IL in ethyl acetate solution (0, 10, and 100 mM). e) Schematic of the perovskite films fabricated using various concentration of the BMIMPF₆ solution for surface treatment.

the concentration of BMIMPF₆ beyond 10 mM, new peaks were observed at $2\theta = 7.92^\circ$, 9.27° (*), and 10.0° (**) (Fig. 5a). These new peaks were assumed to be generated from the formation of perovskite–BMIMPF₆ complex [76,77] rather than the dimensionality conversion of perovskite from 3D to 2D or 1D. Compared to the previously reported phenethylammonium halides, *n*-hexyltrimethylammonium halides [25], and octylammonium halides surface modifiers [24], the BMIMPF₆ IL was composed of bulky ions without the constituent ions of perovskite crystals, and its cation and anion could simultaneously provide the passivation of perovskite. In order to examine for the reactivity of BMIMPF₆ with PbI₂, the films were prepared from the BMIMPF₆ and PbI₂ mixture in DMF/DMSO solution (one-step) or the treatment of BMIMPF₆ on the top of PbI₂ film (two-step). However, any new peaks below 20° region below $\sim 10^\circ$ which corresponded to the formation of low-dimension perovskite were not observed as shown in Fig. S6. Furthermore, at BMIMPF₆ concentrations below 2.5 mM, there were no

distinct variations in the (110) plane of the IL-treated perovskite films (Fig. 5b). This indicates that the 2.5 mM BMIMPF₆ treatment had no significant effect on the original crystal structure within the perovskite film. However, with a further increase in the IL concentration above 5 mM, the (110) peak of perovskite shifted from 14.16° to 14.27° (Fig. 5c), which was also observed for the (220) peak. This was attributed to the deterioration of perovskite crystal by the penetration of excess IL. The conversion of crystals in the perovskite layer after the penetration of the excess amount of IL was also supported by the variations in the surface morphologies, as shown in Fig. 5d. Particularly, a new rod-like phase was observed on the surface of the IL-treated perovskite at concentrations above 5 mM, which verified the conversion of perovskite crystal by the excess IL, and this transformed crystals tended to provide the increased roughness and grain size of the IL-surface treated films at concentrations above 5 mM (Fig. S7 and S8). The XRD spectra of the perovskites were further analyzed by fitting the (110) peak with

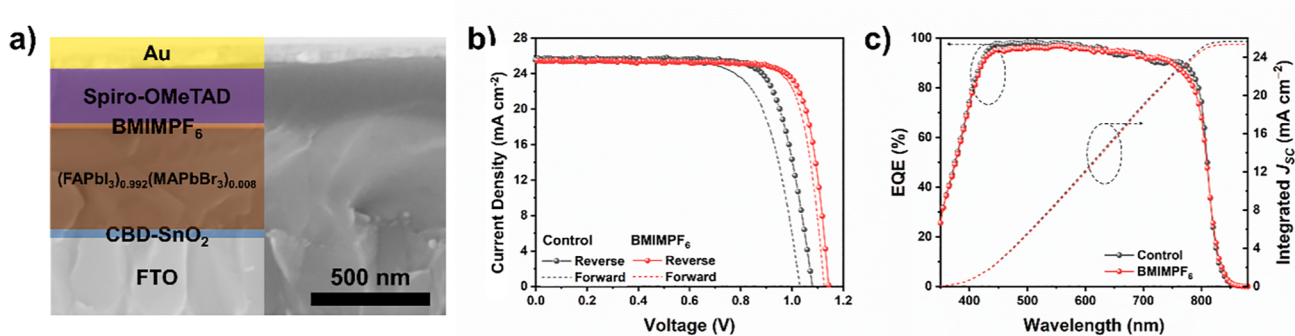


Fig. 6. Cross-sectional SEM image of $(\text{FAPbI}_3)_{0.992}(\text{MAPbBr}_3)_{0.008}$ PPV with the device architecture of FTO/chemical bath deposition-SnO₂/perovskite/Spiro-OMeTAD/Au. b) J - V characteristics of $(\text{FAPbI}_3)_{0.992}(\text{MAPbBr}_3)_{0.008}$ PPVs before and after the BMIMPF₆ treatment measured under AM 1.5G (100 mW cm^{-2}). d) Corresponding EQE spectra of the control and BMIMPF₆-treated $(\text{FAPbI}_3)_{0.992}(\text{MAPbBr}_3)_{0.008}$ PPVs.

Table 2

Photovoltaic parameters of the control and BMIMPF₆-treated $(\text{FAPbI}_3)_{0.992}(\text{MAPbBr}_3)_{0.008}$ PPVs measured under AM 1.5G illumination (100 mW cm^{-2}).

Surface treatment	Scan direction	V_{OC} [V]	J_{SC} [mA cm^{-2}]	FF [%]	PCE [%]	R-F average PCE [%]
Control	Rev	1.08	25.6	76.9	21.2	20.1
	Fwd	1.03	25.7	71.4	18.9	
BMIMPF ₆	Rev	1.14	25.4	80.9	23.5	23.2
	Fwd	1.13	25.4	80.3	23.0	

Gaussian function to extract the microstrain of the plane. As shown in Table S5, reduced microstrain were observed in the BMIMPF₆-treated perovskite films, which corresponded to the reduction of traps [78]. However, this reduced microstrain after the BMIMPF₆ treatment could not offer a reduced bandgap of perovskite caused by mitigating bandtail broadening. In contrast, an increase in the optical band gaps of the BMIMPF₆ IL-treated perovskites was observed (Fig. S9), which may be attributed to the formation of perovskite–IL complex. These results demonstrated that the selective reconstruction and passivation of perovskite surface by the quantitative control of IL is critical for achieving highly efficient PPVs. In addition, it also suggested that the formation of perovskite–IL complex by the penetration of ILs into the perovskite layer could be accelerated when the perovskite surface is exposed to an excess amount of IL, and this would hinder efficient charge transport and extraction to HTL in PPVs despite the enlarged grain size and reduced microstrain (Fig. 5e).

Lastly, the PPVs fabricated using the different perovskite compositions of $((\text{FAPbI}_3)_{0.992}(\text{MAPbBr}_3)_{0.008})$ were prepared and their photovoltaics properties were examined under AM 1.5G (100 mW cm^{-2}) illumination to verify the generality of the perovskite surface reconstruction through IL treatment for efficient PPVs (Fig. 6a). The reduced amount of MAPbBr₃ as a stabilizer [3] and the absence of Cs⁺ would enable the perovskite to possess a wider range of optical absorption up to $\sim 840 \text{ nm}$, which is more ideal for harvesting sunlight energy compared to CsMAFA perovskite. Furthermore, we also employed the CBD method for the homogeneous and compact deposition of SnO₂ ETL accompanied by the reduced density of oxide traps, resulting in the enhanced V_{OC} of PPVs [3,79,80]. As shown in Fig. 6b and Table 2, the BMIMPF₆-treated PPV exhibited an improved PCE of 23.5% with a V_{OC} of 1.14 V and FF of 80.9% and a reduced hysteresis compared to those of the control device (PCE = 21.2 %, $V_{\text{OC}} = 1.08 \text{ V}$, FF = 76.9 %), which may be attributed to the reduced traps and the suppressed charge recombination at the perovskite/HTL after the IL treatment. The statistical data of $(\text{FAPbI}_3)_{0.992}(\text{MAPbBr}_3)_{0.008}$ PPVs are summarized in Fig. S10 and Table S6. Fig. 6c shows the EQE spectra of $(\text{FAPbI}_3)_{0.992}(\text{MAPbBr}_3)_{0.008}$ PPVs. The calculated J_{SC} from the integrations of the EQE spectra of the control and BMIMPF₆-treated PPVs were 25.7

and 25.3 mA cm^{-2} , respectively. The consistencies between the J_{SC} values from the J - V curves and EQE spectra demonstrate the reliability of the J - V measurement used in this study.

4. Conclusions

In summary, we demonstrated the improved performance of PPVs through the post-treatment of perovskite surface with BMIMPF₆ IL. We ascribed this improvement to the reduced trap density and charge recombination via the passivation of the A-site and X-site defects at the perovskite/HTL interface after the IL treatment. The optimally BMIMPF₆-treated PPVs provided increased PCEs of 34.8% and 23.2% for indoor and outdoor conditions, respectively, compared to those of the control devices (30.1% and 20.1%, respectively). In addition, we found that the use of an excess amount of IL could result in the formation of a perovskite–IL complex through the diffusion of the IL into the perovskite layer, leading to inefficient charge transport and extraction in PPVs. Therefore, we suggested that the surface of perovskite should be selectively treated to prevent the penetration of excess amount of the modifier when IL is used as surface modifier to achieve high performance PPVs. This study presents the significant reconstruction of perovskite during exposure to ionic chemicals, and can be used for future development of surface modifiers for perovskite electronics.

Declaration of Competing Interest

The authors declare that they have no known competing financial interests or personal relationships that could have appeared to influence the work reported in this paper.

Acknowledgements

This work was supported by the National Research Foundation of Korea (NRF) grant funded by the Korea government (Ministry of Science and ICT, MSIT) (NRF-2020R1G1A1011577 and NRF-2022R1C1C1004448).

Appendix A. Supplementary data

Supplementary data to this article can be found online at <https://doi.org/10.1016/j.cej.2022.137351>.

References

- [1] H. Min, D.Y. Lee, J. Kim, G. Kim, K.S. Lee, J. Kim, M.J. Paik, Y.K. Kim, K.S. Kim, M.G. Kim, T.J. Shin, S. Il Seok, Perovskite solar cells with atomically coherent interlayers on SnO₂ electrodes, *Nature* 598 (7881) (2021) 444–450.
- [2] J. Jeong, M. Kim, J. Seo, H. Lu, P. Ahlawat, A. Mishra, Y. Yang, M.A. Hope, F.T. Eickemeyer, M. Kim, Y.J. Yoon, I.W. Choi, B.P. Darwich, S.J. Choi, Y. Jo, J.H. Lee, B. Walker, S.M. Zakeeruddin, L. Emsley, U. Rothlisberger, A. Hagfeldt, D.

- S. Kim, M. Grätzel, J.Y. Kim, Pseudo-halide anion engineering for α -FAPbI₃ perovskite solar cells, *Nature* 592 (2021) 381–385, <https://doi.org/10.1038/s41586-021-03406-5>.
- [3] J.J. Yoo, G. Seo, M.R. Chua, T.G. Park, Y. Lu, F. Rotermund, Y.-K. Kim, C.S. Moon, N.J. Jeon, J.-P. Correa-Baena, V. Bulović, S.S. Shin, M.G. Bawendi, J. Seo, Efficient perovskite solar cells via improved carrier management, *Nature* 590 (2021) 587–593, <https://doi.org/10.1038/s41586-021-03285-w>.
- [4] X. He, J. Chen, X. Ren, L. Zhang, Y. Liu, J. Feng, J. Fang, K. Zhao, S. Liu, 40.1% Record low-light solar-cell efficiency by holistic trap-passivation using micrometer-thick perovskite film, *Adv. Energy Mater.* 33 (2021) 2100770, <https://doi.org/10.1002/adma.202100770>.
- [5] J.H. Lee, H.C. Kang, J.-J. Lee, J.W. Jo, Concentrated perovskite photovoltaics enable minimization of energy loss below 0.5 eV under artificial light-emitting diode illumination, *Int. J. Energy Res.* 46 (2022) 5260–5268, <https://doi.org/10.1002/er.7449>.
- [6] S.D. Wolf, J. Holovsky, S.-J. Moon, P. Löper, B. Niesen, M. Ledinsky, F.-J. Haug, J.-H. Yum, C. Ballif, Organometallic halide perovskites: Sharp optical absorption edge and its relation to photovoltaic performance, *J. Phys. Chem. Lett.* 5 (2014) 1035–1039, <https://doi.org/10.1021/jz500279b>.
- [7] L.M. Herz, Charge-carrier mobilities in metal halide perovskites: Fundamental mechanisms and limits, *ACS Energy Lett.* 2 (2017) 1539–1548, <https://doi.org/10.1021/acsenergylett.7b00276>.
- [8] E.J. Juarez-Perez, R.S. Sanchez, L. Badia, G. Garcia-Belmonte, Y.S. Kang, I. Mora-Sero, J. Bisquert, Photoinduced giant dielectric constant in lead halide perovskite solar cells, *J. Phys. Chem. Lett.* 5 (2014) 2390–2394, <https://doi.org/10.1021/jz5011169>.
- [9] S.D. Stranks, G.E. Eperon, G. Grancini, C. Menelaou, M.J.P. Alcocer, T. Leijtens, L. M. Herz, A. Petrozza, H.J. Snaith, Electron-hole diffusion lengths exceeding 1 micrometer in an organometal trihalide perovskite absorber, *Science* 342 (2013) 341–344, <https://doi.org/10.1126/science.1243982>.
- [10] F. Giordano, A. Abate, J.-P. Correa-Baena, M. Saliba, T. Matsui, S.H. Im, S. M. Zakeeruddin, M.K. Nazeeruddin, A. Hagfeldt, M. Grätzel, Enhanced electronic properties in mesoporous TiO₂ via lithium doping for high-efficiency perovskite solar cells, *Nature Commun.* 7 (2016) 10379, <https://doi.org/10.1038/ncomms10379>.
- [11] Q. Jiang, L. Zhang, H. Wang, X. Yang, J. Meng, H. Liu, Z. Yin, J. Wu, X. Zhang, J. You, Enhanced electron extraction using SnO₂ for high-efficiency planar-structure H(NH₂)₂PbI₃-based perovskite solar cells, *Nat. Energy* 2 (2016) 16177, <https://doi.org/10.1038/nenergy.2016.177>.
- [12] H. Tan, A. Jain, O. Voznyi, X. Lan, F.P. García de Arquer, J.Z. Fan, R. Quintero-Bermudez, M. Yuan, B. Zhang, Y. Zhao, F. Fan, P. Li, L.N. Quan, Y. Zhao, Z.-H. Lu, Z. Yang, S. Hoogland, E.H. Sargent, Efficient and stable solution-processed planar perovskite solar cells via contact passivation, *Science* 355 (2017) 722–726, <https://doi.org/10.1126/science.aai9081>.
- [13] N.J. Jeon, H. Na, E.H. Jung, T.-Y. Yang, Y.G. Lee, G. Kim, H.-W. Shin, S.I. Seok, J. Lee, J. Seo, A fluorene-terminated hole-transporting material for highly efficient and stable perovskite solar cells, *Nat. Energy* 3 (2018) 682–689, <https://doi.org/10.1038/s41560-018-0200-6>.
- [14] M. Jeong, I.W. Choi, E.M. Go, Y. Cho, M. Kim, B. Lee, S. Jeong, Y. Jo, H.W. Choi, J. Lee, J.-H. Bae, S.K. Kwak, D.S. Kim, C. Yang, Stable perovskite solar cells with efficiency exceeding 24.8% and 0.3-V voltage loss, *Science* 369 (6511) (2020) 1615–1620.
- [15] M. Jeong, I.W. Choi, K. Yim, S. Jeong, M. Kim, S.J. Choi, Y. Cho, J.-H. An, H.-B. Kim, Y. Jo, S.-H. Kang, J.-H. Bae, C.-W. Lee, D.S. Kim, C. Yang, Large-area perovskite solar cells employing spiro-Naph hole transport material, *Nat. Photonics* 16 (2022) 119–125, <https://doi.org/10.1038/s41566-021-00931-7>.
- [16] J. Chen, N.-G. Park, Materials and methods for interface engineering toward stable and efficient perovskite solar cells, *ACS Energy Lett.* 5 (2020) 2742–2786, <https://doi.org/10.1021/acsenergylett.0c01240>.
- [17] Y. Wu, H. Zhu, B.-B. Yu, S. Akin, Y. Liu, Z. Shen, L. Pan, H. Cai, Interface modification to achieve high-efficiency and stable perovskite solar cells, *Chem. Eng. J.* 433 (2022), 134613, <https://doi.org/10.1016/j.cej.2022.134613>.
- [18] S. Yuan, T. Zhang, H. Chen, Y. Ji, Y. Hao, H. Zheng, Y. Wang, Z.D. Chen, L. Chen, S. Li, Dual-functional passivators for highly efficient and hydrophobic FA-based perovskite solar cells, *Chem. Eng. J.* 433 (2022), 133227, <https://doi.org/10.1016/j.cej.2021.133227>.
- [19] W.-M. Gu, K.-J. Jiang, F. Li, G.-H. Yu, Y. Xu, X.-H. Fan, C.-Y. Gao, L.-M. Yang, Y. Song, A multifunctional interlayer for highly stable and efficient perovskite solar cells based on pristine poly(3-hexylthiophene), *Chem. Eng. J.* 444 (2022), 136644, <https://doi.org/10.1016/j.cej.2022.136644>.
- [20] C. Wang, X. Wang, Z. He, B. Zhou, D. Qu, Y. Wang, H. Hu, Q. Hu, Y. Tu, Minimizing voltage deficit in methylammonium-free perovskite solar cells via surface reconstruction, *Chem. Eng. J.* 444 (2022), 136622, <https://doi.org/10.1016/j.cej.2022.136622>.
- [21] Y. Hu, W. Song, X. Wang, X. Shu, X. Jia, Z. He, S. Zhang, G. Yuan, M. Wang, J. Wang, G. Sun, T. Sun, Y. Tang, A holistic sunscreen interface strategy to effectively improve the performance of perovskite solar cells and prevent lead leakage, *Chem. Eng. J.* 433 (2022), 134566, <https://doi.org/10.1016/j.cej.2022.134566>.
- [22] G. Wu, R. Liang, M. Ge, G. Sun, Y. Zhang, G. Xing, Surface passivation using 2D perovskites toward efficient and stable perovskite solar cells, *Adv. Mater.* 34 (2022) 2105635, <https://doi.org/10.1002/adma.202105635>.
- [23] Q. Jiang, Y. Zhao, X. Zhang, X. Yang, Y. Chen, Z. Chu, Q. Ye, X. Li, Z. Yin, J. You, Surface passivation of perovskite film for efficient solar cells, *Nat. Photonics* 13 (2019) 460–466, <https://doi.org/10.1038/s41566-019-0398-2>.
- [24] J.J. Yoo, S. Wieghold, M.C. Sponseller, M.R. Chua, S.N. Bertram, N.T.P. Hartono, J. S. Tresback, E.C. Hansen, J.-P. Correa-Baena, V. Bulović, T. Buonassisi, S.S. Shin, M.G. Bawendi, An interface stabilized perovskite solar cell with high stabilized efficiency and low voltage loss, *Energy Environ. Sci.* 12 (7) (2019) 2192–2199.
- [25] E.H. Jung, N.J. Jeon, E.Y. Park, C.S. Moon, T.J. Shin, T.-Y. Yang, J.H. Noh, J. Seo, Efficient, stable and scalable perovskite solar cells using poly(3-hexylthiophene), *Nature* 567 (2019) 511–515, <https://doi.org/10.1038/s41586-019-1036-3>.
- [26] Q. Wang, Q. Dong, T. Li, A. Gruber, J. Huang, Thin insulating tunneling contacts for efficient and water-resistant perovskite solar cells, *Adv. Mater.* 28 (2016) 6734–6739, <https://doi.org/10.1002/adma.201600969>.
- [27] B. Chaudhary, A. Kulkarni, A.K. Jena, M. Ikegami, Y. Udagawa, H. Kunugita, K. Ema, T. Miyasaka, Poly(4-Vinylpyridine)-based interfacial passivation to enhance voltage and moisture stability of lead halide perovskite solar cells, *ChemSusChem* 10 (2017) 2473–2479, <https://doi.org/10.1002/cssc.201700271>.
- [28] S.-H. Turren-Cruz, A. Hagfeldt, M. Saliba, Methylammonium-free, high-performance, and stable perovskite solar cells on a planar architecture, *Science* 362 (2018) 449–453, <https://doi.org/10.1126/science.aat3583>.
- [29] A. Capasso, F. Matteocci, L. Najafi, M. Prato, J. Buha, L. Cinà, V. Pellegrini, A. D. Carlo, F. Bonacorso, Few-layer MoS₂ flakes as active buffer layer for stable perovskite solar cells, *Adv. Energy Mater.* 6 (2016) 1600920, <https://doi.org/10.1002/aenm.201600920>.
- [30] F. Cheng, R. He, S. Nie, C. Zhang, J. Yin, J. Li, N. Zheng, B. Wu, Perovskite quantum dots as multifunctional interlayers in perovskite solar cells with dopant-free organic hole transporting layers, *J. Am. Chem. Soc.* 143 (2021) 5855–5866, <https://doi.org/10.1021/jacs.1c00852>.
- [31] A. Abate, M. Saliba, D.J. Hollman, S.D. Stranks, K. Wojciechowski, R. Avolio, G. Grancini, A. Petrozza, H.J. Snaith, Supramolecular halogen bond passivation of organic-inorganic halide perovskite solar cells, *Nano Lett.* 14 (2014) 3247–3254, <https://doi.org/10.1021/nl500627x>.
- [32] Y. Lin, L. Shen, J. Dai, Y. Deng, Y. Wu, Y. Bai, X. Zheng, J. Wang, Y. Fang, H. Wei, W. Ma, X.C. Zeng, X. Zhan, J. Huang, π -Conjugated lewis base: Efficient trap-passivation and charge-extraction for hybrid perovskite solar cells, *Adv. Mater.* 29 (2017) 1604545, <https://doi.org/10.1002/adma.201604545>.
- [33] R.J.E. Westbrook, T.J. Macdonald, W. Xu, L. Lanzetta, J.M. Marin-Beloqui, T. M. Clarke, S.A. Haque, Lewis base passivation mediates charge transfer at perovskite heterojunctions, *J. Am. Chem. Soc.* 143 (2021) 12230–12243, <https://doi.org/10.1021/jacs.1c05122>.
- [34] M. Abdi-Jalebi, M.I. Dar, S.P. Senanayak, A. Sadhanala, Z. Andaji-Garmaroudi, L. M. Pazos-Outón, J.M. Richter, A.J. Pearson, H. Sirringhaus, M. Grätzel, R. H. Friend, Charge extraction via graded doping of hole transport layers gives highly luminescent and stable metal halide perovskite devices, *Sci. Adv.* 5 (2019) eaav2012, <https://doi.org/10.1126/sciadv.aav2012>.
- [35] P. Cui, D. Wei, J. Ji, H. Huang, E. Jia, S. Dou, T. Wang, W. Wang, M. Li, Planar p–n homojunction perovskite solar cells with efficiency exceeding 21.3%, *Nat. Energy* 4 (2) (2019) 150–159.
- [36] Y.-W. Jang, S. Lee, K.M. Yeom, K. Jeong, K. Choi, M. Choi, J.H. Noh, Intact 2D/3D halide junction perovskite solar cells via solid-phase in-plane growth, *Nat. Energy* 6 (2021) 63–71, <https://doi.org/10.1038/s41560-020-00749-7>.
- [37] L. Zhu, X. Zhang, M. Li, X. Shang, K. Lei, B. Zhang, C. Chen, S. Zheng, H. Song, J. Chen, Trap state passivation by rational ligand molecule engineering toward efficient and stable perovskite solar cells exceeding 23% efficiency, *Adv. Energy Mater.* 11 (2021) 2100529, <https://doi.org/10.1002/aenm.202100529>.
- [38] T. Niu, L. Chao, W. Gao, C. Ran, L. Song, Y. Chen, L. Fu, W. Huang, Ionic liquids-enabled efficient and stable perovskite photovoltaics: Progress and challenges, *ACS Energy Lett.* 6 (2021) 1453–1479, <https://doi.org/10.1021/acsenergylett.0c02696>.
- [39] J.-Y. Seo, T. Matsui, J. Luo, J.-P. Correa-Baena, F. Giordano, M. Saliba, K. Schenck, A. Ummadisingu, K. Domanski, M. Hadadian, A. Hagfeldt, S.M. Zakeeruddin, U. Steiner, M. Grätzel, A. Abate, Ionic liquid control crystal growth to enhance planar perovskite solar cells efficiency, *Adv. Energy Mater.* 5 (2016) 1600767, <https://doi.org/10.1002/aenm.201600767>.
- [40] L. Chao, Y. Xia, B. Li, G. Xing, Y. Chen, W. Huang, Room-temperature molten salt for facile fabrication of efficient and stable perovskite solar cells in ambient air, *Chem* 5 (2019) 995–1006, <https://doi.org/10.1016/j.chempr.2019.02.025>.
- [41] S. Akin, E. Akman, S. Sonmezoglu, FAPbI₃-based perovskite solar cells employing hexyl-based ionic liquid with an efficiency over 20% and excellent long-term stability, *Adv. Funct. Mater.* 30 (2020) 2002964, <https://doi.org/10.1002/adfm.202002964>.
- [42] Q. Wu, W. Zhou, Q. Liu, P. Zhou, T. Chen, Y. Lu, Q. Qiao, S. Yang, Solution-processable ionic liquid as an independent or modifying electron transport layer for high-efficiency perovskite solar cells, *ACS Appl. Mater. Interfaces* 8 (2016) 34464–34473, <https://doi.org/10.1021/acsmami.6b12683>.
- [43] C. Huang, P. Lin, N. Fu, K. Sun, M. Ye, C. Liu, X. Zhou, L. Shu, X. Hao, B. Xu, X. Zeng, Y. Wang, S. Ke, Ionic liquid modified SnO₂ nanocrystals as a robust electron transporting layer for efficient planar perovskite solar cells, *J. Mater. Chem. A* 6 (2018) 22086–22095, <https://doi.org/10.1039/C8TA04131H>.
- [44] X. Zhou, M. Hu, C. Liu, L. Zhang, X. Zhong, X. Li, Y. Tian, C. Cheng, B. Xu, Synergistic effects of multiple functional ionic liquid-treated PEDOT:PSS and less-ion-defects S-acetylthiocholine chloride-passivated perovskite surface enabling stable and hysteresis-free inverted perovskite solar cells with conversion efficiency over 20%, *Nano Energy* 63 (2019), 103866 <https://doi.org/10.1016/j.nanoen.2019.103866>.
- [45] M. Du, X. Zhu, L. Wang, H. Wang, J. Feng, X. Jiang, Y. Cao, Y. Sun, L. Duan, Y. Jiao, K. Wang, X. Ren, Z. Yan, S. Pang, S. Liu, High-pressure nitrogen-extraction and effective passivation to attain highest large-area perovskite solar module

- efficiency, *Adv. Mater.* 32 (2020) 2004979, <https://doi.org/10.1002/adma.202004979>.
- [46] X. Zhu, M. Du, J. Feng, H. Wang, Z. Xu, L. Wang, S. Zuo, C. Wang, Z. Wang, C. Zhang, X. Ren, S. Priya, D. Yang, S. Liu, High-efficiency perovskite solar cells with imidazolium-based ionic liquid for surface passivation and charge transport, *Angew. Chem. Int. Ed.* 60 (2021) 4238–4244, <https://doi.org/10.1002/anie.202010987>.
- [47] X. Zhu, S. Yang, Y. Cao, L. Duan, M. Du, J. Feng, Y. Jiao, X. Jiang, Y. Sun, H. Wang, S. Zuo, Y. Liu, S. Liu, Ionic-liquid-perovskite capping layer for stable 24.33%-efficient solar cell, *Adv. Energy Mater.* 12 (2021) 2103491, <https://doi.org/10.1002/aenm.202103491>.
- [48] M. Salado, A.D. Jodlowski, C. Roldan-Carmona, G. de Miguel, S. Kazim, M. K. Nazeeruddin, S. Ahmad, Surface passivation of perovskite layers using heterocyclic halides: Improved photovoltaic properties and intrinsic stability, *Nano Energy* 50 (2018) 220–228, <https://doi.org/10.1016/j.nanoen.2018.05.035>.
- [49] X. Zhong, Z. Liu, D. Cao, Improved united-atom force field for imidazolium-based ionic liquids: tetrafluoroborate, hexafluorophosphate, methylsulfate, trifluoromethylsulfonate, acetate, trifluoroacetate, and bis(trifluoromethylsulfonyl)amide, *J. Phys. Chem. B* 115 (2011) 10027–10040, <https://doi.org/10.1021/jp204148q>.
- [50] Y. Zhang, E.J. Maginn, The effect of C2 substitution on melting point and liquid phase dynamics of imidazolium based-ionic liquids: insights from molecular dynamics simulations, *PCCP* 14 (2012) 12157–12164, <https://doi.org/10.1039/C2CP41964E>.
- [51] J. Xu, J. Cui, S. Yang, Y. Han, X. Guo, Y. Che, D. Xu, C. Duan, W. Zhao, K. Guo, W. Ma, B. Xu, J. Yao, Z. Liu, S. Liu, Unraveling passivation mechanism of imidazolium-based ionic liquids on inorganic perovskite to achieve near-record-efficiency CsPbI₂Br solar cells, *Nano-Micro Lett.* 14 (2022) 7, <https://doi.org/10.1007/s40820-021-00763-8>.
- [52] X. Liu, H. Lian, Z. Zhou, C. Zou, J. Xie, F. Zhang, H. Yuan, S. Yang, Y. Hou, H. G. Yang, Stoichiometric dissolution of defective CsPbI₂Br surfaces for inorganic solar cells with 17.5% efficiency, *Adv. Energy Mater.* 12 (2022) 2103933, <https://doi.org/10.1002/aenm.202103933>.
- [53] M. Peng, W. Dai, L. Lin, B. Xiao, S. Guo, M. Fang, H. Wang, Y. Gou, M.S. Irshad, J. Gong, J. Li, Performance improvement of perovskite solar cells by using ionic liquid BMIMPF₆ as an interface modifier, *ACS Appl. Energy Mater.* 4 (2021) 12421–12428, <https://doi.org/10.1021/acsam.1c02248>.
- [54] R. Yin, K.-X. Wang, S. Cui, B.-B. Fan, J.-W. Liu, Y.-K. Gao, T.-T. You, P.-G. Yin, Dual-interface modification with BMIMPF₆ for high-efficiency and stable carbon-based CsPbI₂Br perovskite solar cells, *ACS Appl. Energy Mater.* 4 (2021) 9294–9303, <https://doi.org/10.1021/acsam.1c01521>.
- [55] Y. Shao, Z. Xiao, C. Bi, Y. Yuan, J. Huang, Origin and elimination of photocurrent hysteresis by fullerene passivation in CH₃NH₃PbI₃ planar heterojunction solar cells, *Nat. Commun.* 5 (2014) 5784, <https://doi.org/10.1038/ncomms6784>.
- [56] T.-S. Su, F.T. Eickemeyer, M.A. Hope, F. Jahanbakhshi, M. Mladenović, J. Li, Z. Zhou, A. Mishra, J.-H. Yum, D. Ren, A. Krishna, O. Ouellette, T.-C. Wei, H. Zhou, H.-H. Huang, M.D. Mensi, K. Sivula, S.M. Zakeeruddin, J.V. Milić, A. Hagfeldt, U. Rothlisberger, L. Emsley, H. Zhang, M. Grätzel, Crown ether modulation enables over 23% efficient formamidinium-based perovskite solar cells, *J. Am. Chem. Soc.* 142 (2020) 19980–19991, <https://doi.org/10.1021/jacs.0c08592>.
- [57] H. Zhu, Y. Ren, L. Pan, O. Ouellette, F.T. Eickemeyer, Y. Wu, X. Li, S. Wang, H. Liu, X. Dong, S.M. Zakeeruddin, Y. Liu, A. Hagfeldt, M. Grätzel, Synergistic effect of fluorinated passivator and hole transport dopant enables stable perovskite solar cells with an efficiency near 24%, *J. Am. Chem. Soc.* 143 (2021) 3231–3237, <https://doi.org/10.1021/jacs.0c12802>.
- [58] W. Zhang, X. Liu, B. He, Z. Gong, J. Zhu, Y. Ding, H. Chen, Q. Tang, Interface engineering of imidazolium ionic liquids toward efficient and stable CsPbBr 3 perovskite solar cells, *ACS Appl. Mater. Interfaces* 12 (2020) 4540–4548, <https://doi.org/10.1021/acsami.9b20831>.
- [59] M. Zhang, Q. Chen, R. Xue, Y. Zhan, C. Wang, J. Lai, J. Yang, H. Lin, J. Yao, Y. Li, L. Chen, Y. Li, Reconfiguration of interfacial energy band structure for high-performance inverted structure perovskite solar cells, *Nat. Commun.* 10 (2019) 4593, <https://doi.org/10.1038/s41467-019-12613-8>.
- [60] H. Kanda, N. Shibayama, A.J. Huckaba, Y. Lee, S. Paek, N. Klipfel, C. Roldán-Carmona, V.I.E. Queloz, G. Grancini, Y.i. Zhang, M. Abuhelaqa, K.T. Cho, M.O. Li, M.D. Mensi, S. Kinge, M.K. Nazeeruddin, Band-bending induced passivation: high performance and stable perovskite solar cells using a perhydropoly(silazane) precursor, *Energy Environ. Sci.* 13 (4) (2020) 1222–1230.
- [61] F. Yang, H.E. Lim, F. Wang, M. Ozaki, A.i. Shimazaki, J. Liu, N.B. Mohamed, K. Shinokita, Y. Miyauchi, A. Wakamiya, Y. Murata, K. Matsuda, Roles of polymer layer in enhanced photovoltaic performance of perovskite solar cells via interface engineering, *Adv. Mater. Interfaces* 5 (3) (2018) 1701256.
- [62] Z. Huang, X. Hu, C. Liu, X. Meng, Z. Huang, J. Yang, X. Duan, J. Long, Z. Zhao, L. Tan, Y. Song, Y. Chen, Water-resistant and flexible perovskite solar cells via a glued interfacial layer, *Adv. Funct. Mater.* 29 (37) (2019) 1902629.
- [63] T. Du, W. Xu, S. Xu, S.R. Ratnasingham, C.-T. Lin, J. Kim, J. Briscoe, M. A. McLachlan, J.R. Durrant, Light-intensity and thickness dependent efficiency of planar perovskite solar cells: charge recombination versus extraction, *J. Mater. Chem. C* 8 (2020) 12648–12655, <https://doi.org/10.1039/D0TC03390A>.
- [64] Z. Li, J. Zhang, S. Wu, X. Deng, F. Li, D. Liu, C.-C. Lee, F. Lin, D. Lei, C.-C. Chueh, Z. Zhu, A.-K.-Y. Jen, Minimized surface deficiency on wide-bandgap perovskite for efficient indoor photovoltaics, *Nano Energy* 78 (2020), 105377, <https://doi.org/10.1016/j.nanoen.2020.105377>.
- [65] W. Tress, M. Yavari, K. Domanski, P. Yadav, B. Niesen, J.-P. Correa-Baena, A. Hagfeldt, M. Grätzel, Interpretation and evolution of open-circuit voltage, recombination, ideality factor and subgap defect states during reversible light-soaking and irreversible degradation of perovskite solar cells, *Energy Environ. Sci.* 11 (2018) 151–165, <https://doi.org/10.1039/C7EE02415K>.
- [66] Z. Wu, M. Jiang, Z. Liu, A. Jamshaid, L.K. Ono, Y. Qi, Highly efficient perovskite solar cells enabled by multiple ligand passivation, *Adv. Energy Mater.* 10 (2020) 1903696, <https://doi.org/10.1002/aenm.201903696>.
- [67] H. Opoku, J.H. Lee, B. Nketia-Yawson, H. Ahn, J.-J. Lee, J.W. Jo, Structurally-tuned benzo[1,2-b:4,5-b']dithiophene-based polymer as a dopant-free hole transport material for perovskite solar cells, *J. Polym. Sci.* 60 (2022) 985–991, <https://doi.org/10.1002/pol.20210400>.
- [68] J.H. Lee, M.H. Jang, C.H. Lee, J.-J. Lee, S.Y. Lee, J.W. Jo, Inclusion of triphenylamine unit in dopant-free hole transport material for enhanced interfacial interaction in perovskite photovoltaics, *Dyes Pigm.* 200 (2022), 110162, <https://doi.org/10.1016/j.dyepig.2022.110162>.
- [69] J. Chen, N.-G. Park, Causes and solutions of recombination in perovskite solar cells, *Adv. Mater.* 31 (2019) 1803019, <https://doi.org/10.1002/adma.201803019>.
- [70] I.S. Yang, N.-G. Park, Dual additive for simultaneous improvement of photovoltaic performance and stability of perovskite solar cell, *Adv. Funct. Mater.* 31 (2021) 2100396, <https://doi.org/10.1002/adfm.202100396>.
- [71] H. Opoku, Y.H. Kim, J.H. Lee, H. Ahn, J.-J. Lee, S.-W. Baek, J.W. Jo, A tailored graft-type polymer as a dopant-free hole transport material in indoor perovskite photovoltaics, *J. Mater. Chem. A* 9 (2021) 15294–15300, <https://doi.org/10.1039/DITA03577K>.
- [72] S. Zhang, H. Si, W. Fan, M. Shi, M. Li, C. Xu, Z. Zhang, Q. Liao, A. Sattar, Z. Kang, Y. Zhang, Graphdiyne: Bridging SnO₂ and perovskite in planar solar cells, *Angew. Chem. Int. Ed.* 59 (2020) 11573–11582, <https://doi.org/10.1002/anie.202003502>.
- [73] C. Xu, Z. Zhang, S. Zhang, H. Si, S. Ma, W. Fan, Z. Xiong, Q. Liao, A. Sattar, Z. Kang, Y. Zhang, Manipulation of perovskite crystallization kinetics via lewis base additives, *Adv. Funct. Mater.* 31 (2021) 2009425, <https://doi.org/10.1002/adfm.202009425>.
- [74] S. Bai, P. Dai, C. Li, Z. Wang, Z. Yuan, F. Fu, M. Kawecki, X. Liu, N. Sakai, J.-T. W. Wang, S. Huettnner, S. Buecheler, M. Fahlman, F. Gao, H.J. Snaith, Planar perovskite solar cells with long-term stability using ionic liquid additives, *Nature* 571 (2019) 245–250, <https://doi.org/10.1038/s41586-019-1357-2>.
- [75] J. Chen, S.-G. Kim, N.-G. Park, FA_{0.88}Cs_{0.12}PbI_{3-x}(PF₆)_x Interlayer formed by ion exchange reaction between perovskite and hole transporting layer for improving photovoltaic performance and stability, *Adv. Mater.* 30 (2018) 1801948, <https://doi.org/10.1002/adma.201801948>.
- [76] A.M.A. Leguy, Y. Hu, M. Campoy-Quiles, M.I. Alonso, O.J. Weber, P. Azarhoosh, M. van Schilfgaarde, M.T. Weller, T. Bein, J. Nelson, P. Docampo, P.R.F. Barnes, Reversible hydration of CH₃NH₃PbI₃ in films, single crystals, and solar cells, *Chem. Mater.* 27 (2015) 3397–3407, <https://doi.org/10.1021/acs.chemmater.5b00660>.
- [77] J. Zhao, B. Cai, Z. Luo, Y. Dong, Y. Zhang, H. Xu, B. Hong, Y. Yang, L. Li, W. Zhang, C. Gao, Investigation of the hydrolysis of perovskite organometallic halide CH₃NH₃PbI₃ in humidity environment, *Sci. Rep.* 6 (2016) 21976, <https://doi.org/10.1038/srep21976>.
- [78] G. Kim, H. Min, K.S. Lee, D.Y. Lee, S.M. Yoon, S.I. Seok, Impact of strain relaxation on performance of α-formamidinium lead iodide perovskite solar cells, *Science* 370 (2020) 108–112, <https://doi.org/10.1126/science.abc4417>.
- [79] E.H. Anaraki, A. Kermanpur, L. Steier, K. Domanski, T. Matsui, W. Tress, M. Saliba, A. Abate, M. Grätzel, A. Hagfeldt, J.-P. Correa-Baena, Highly efficient and stable planar perovskite solar cells by solution-processed tin oxide, *Energy Environ. Sci.* 9 (2016) 3128–3134, <https://doi.org/10.1039/C6EE02390H>.
- [80] J. Zhang, C. Bai, Y. Dong, W. Shen, Q. Zhang, F. Huang, Y.-B. Cheng, J. Zhong, Batch chemical bath deposition of large-area SnO₂ film with mercaptosuccinic acid decoration for homogenized and efficient perovskite solar cells, *Chem. Eng. J.* 425 (2021), 131444, <https://doi.org/10.1016/j.cej.2021.131444>.